

## Charge-transfer-induced interfacial ferromagnetism in $\text{La}_{0.7}\text{Sr}_{0.3}\text{MnO}_3/\text{NdNiO}_3$

K. Chen<sup>1,\*</sup>, C. Luo<sup>1</sup>, B. B. Chen<sup>2</sup>, R. M. Abrudan<sup>1</sup>, G. Koster<sup>2</sup>, S. K. Mishra<sup>3</sup>, and F. Radu<sup>1,†</sup>

<sup>1</sup>*Helmholtz-Zentrum Berlin für Materialien und Energie, Albert-Einstein-Strasse 15, 12489 Berlin, Germany*

<sup>2</sup>*MESA+ Institute for Nanotechnology, University of Twente, 7522 NH Enschede, The Netherlands*

<sup>3</sup>*School of Material Science and Technology, Indian Institute of Technology (BHU), Varanasi 221005, India*



(Received 23 October 2019; revised manuscript received 3 April 2020; accepted 27 April 2020; published 12 May 2020)

Charge-transfer-induced interfacial ferromagnetism and its impact on the exchange bias effect in  $\text{La}_{0.7}\text{Sr}_{0.3}\text{MnO}_3/\text{NdNiO}_3$  correlated oxide heterostructures were investigated by soft x-ray absorption and x-ray magnetic circular dichroism spectra in a temperature range from 10 to 300 K. Besides the antiferromagnetic  $\text{Ni}^{3+}$  cations which are naturally part of the  $\text{NdNiO}_3$  layer,  $\text{Ni}^{2+}$  ions are formed at the interface due to a charge-transfer mechanism involving the Mn element of the adjacent layer. They exhibit a ferromagnetic behavior due to the exchange coupling to the  $\text{Mn}^{4+}$  ions in the  $\text{La}_{0.7}\text{Sr}_{0.3}\text{MnO}_3$  layer. This can be seen as detrimental to the strength of the unidirectional anisotropy since a significant part of the interface does not contribute to the pinning of the ferromagnetic layer. By analyzing the line-shape changes of the x-ray absorption at the Ni  $L_{2,3}$  edges, the metal-insulator transition of the  $\text{NdNiO}_3$  layer is resolved in an element-specific manner. This phase transition is initiated at about 120 K, way above the paramagnetic to antiferromagnetic transition of the  $\text{NdNiO}_3$  layer which measured to be 50 K. Exchange bias and enhanced coercive fields were observed after field cooling the sample through the Néel temperature of the  $\text{NdNiO}_3$  layer. Different from  $\text{La}_{0.7}\text{Sr}_{0.3}\text{MnO}_3/\text{LaNiO}_3$ , the exchange bias observed in  $\text{La}_{0.7}\text{Sr}_{0.3}\text{MnO}_3/\text{NdNiO}_3$  is due to the antiferromagnetism of  $\text{NdNiO}_3$  and the frustration at the interface. These results suggest that reducing the interfacial orbital hybridization may be used as a tunable parameter for the strength of the exchange bias effect in all-oxide heterostructures which exhibit a charge-transfer mechanism.

DOI: 10.1103/PhysRevMaterials.4.054408

### I. INTRODUCTION

Electronic reconstruction at oxide interfaces [1], has been intensively investigated to explain the appearance of novel properties in layered structures, such as the ferromagnetic metallic state at the interface of  $\text{LaAlO}_3/\text{SrTiO}_3$  [2–5], and the interfacial two-dimensional electron gas in  $\text{LaAlO}_3/\text{SrTiO}_3$  [6] and  $\gamma\text{-Al}_2\text{O}_3/\text{SrTiO}_3$  [7,8] systems. Oxygen vacancies [9–11], structural strains [12], and charge redistributions [13] in the atomic layers close to the interfaces have been established as underlying mechanisms for the complex traits of oxide-based heterostructures. A sharp bandwidth-controlled metal-insulator transition (MIT) [14] has been widely observed in the  $R\text{NiO}_3$  nickelate oxides (both in bulk and films) with smaller lanthanide ions ( $R \neq \text{La}$ ), accompanied by a transition from paramagnetic to antiferromagnetic (AFM) state as a function of temperature. Charge-transfer and orbital reconstruction mechanisms that occur at the interface serve as the basic mechanisms for numerous fascinating phenomena that have been observed in ferromagnetic (FM)/ $R\text{NiO}_3$  heterostructures, such as metal-insulator-metal transition in  $\text{CoFe}_2\text{O}_4/\text{NdNiO}_3$  [15], exchange bias effect [16,17], noncollinear magnetic structure [18], and superconductivity [19] in  $\text{La}_{1-x}\text{Sr}_x\text{MnO}_3/\text{LaNiO}_3$  (LSMO/LNO).

Moreover, the charge transfer at the  $\text{La}_{0.8}\text{Sr}_{0.2}\text{MnO}_3/\text{NdNiO}_3$  interface can be controlled via strain engineering [20].

For the charge-transfer scenario of the  $\text{La}_{0.7}\text{Sr}_{0.3}\text{MnO}_3/\text{NdNiO}_3$  (LSMO/NNO) bilayer, hole transfer from  $\text{Ni}^{3+}$  to  $\text{Mn}^{3+}$  would result in  $\text{Ni}^{2+}$  and  $\text{Mn}^{4+}$  at the interface favoring the ferromagnetic  $\text{Ni}^{2+}\text{-O}^{2-}\text{-Mn}^{4+}$  interactions, similar to that observed in  $\text{La}_2\text{NiMnO}_6$  [21,22]. Such an interfacial ferromagnetism of  $\text{Ni}^{2+}$  has been observed in  $(\text{LaNiO}_3)_n/(\text{LaMnO}_3)_2$  superlattices [23]. The FM interaction between  $\text{Ni}^{2+}$  and  $\text{Mn}^{4+}$  which are further coupled to the antiferromagnetic  $\text{Ni}^{3+}$  ions in the buried  $\text{NdNiO}_3$  layer, give rise to frustrated magnetic regions that affect the coercive and the exchange bias field of the FM layer [12,24,25]. An exchange bias effect is conventionally observed for a ferromagnetic layer which shares a common interface with an antiferromagnetic one. As such, the NNO layer can be used as the antiferromagnetic bias layer which mediates an eventual occurrence of interfacial unidirectional anisotropy. By contrast, LNO is Pauli paramagnetic, therefore it is not expected that this magnetic ground state will support the formation of an unidirectional anisotropy. Nevertheless, by surprise, an exchange bias was observed in LSMO/LNO [16,17,20], and it is yet unclear what is the underlying mechanism and if it offers sufficient tunability of the unidirectional magnetic anisotropy. By contrast, the NNO thin films do exhibit an antiferromagnetic ground state which may be optimized against strain, dimensionality, and other intrinsic and extrinsic constraints [26–35].

\*kaichen.hzg@gmail.com

†florin.radu@helmholtz-berlin.de

In this paper we report on the complexity of the magnetic interactions that occur at the interface, revealing correlations between the unidirectional anisotropy, charge transfer, interfacial exchange coupling, and the metal-insulator transition in LSMO/NNO heterostructures. In the next section we introduce the samples and describe their structural, magnetic, and transport properties measured by means of laboratory tools. In the third section we make use of soft x-ray spectroscopy to reveal an interfacial charge transfer between the constituent Mn and Ni elements, and demonstrate the occurrence of the MIT phase transition for the NNO layer. By analyzing the XAS at the Mn edge for two different thicknesses of the LSMO layer, we bring compelling evidence for a valence gradient of the Mn element towards the interface. Moreover, by analyzing the peak positions in the x-ray absorption spectroscopy (XAS) spectra measured across the Ni  $L_{2,3}$  resonant edges, we observe the formation of  $\text{Ni}^{2+}$ . By corroborating these two observations, we are able to fully demonstrate the occurrence of a charge-transfer effect at the LSMO/NNO interface. Furthermore, by analyzing the profile of the XAS spectra which were measured as a function of temperature, we clearly reveal the occurrence of the MIT phase transition which initiates at 120 K. In the fourth section we involve x-ray magnetic circular dichroism measured at the Mn, Ni, and Nd edges measured as a function of temperature, and as a function of an external magnetic field reaching up to 8 Tesla. X-ray magnetic circular dichroism (XMCD) measured for the Mn layer as a function of temperature provides the Curie temperature of the FM layer which was 180 K. Through the XMCD measurements as a function of an external field and as a function of temperature at the Nd  $M_{5,4}$  resonant edges, we are able to measure the Néel temperature of the AFM NNO layer, which is equal to 50 K for our system. The measurement of the three critical temperatures within the same methodical environment for the same sample is an important ingredient for disentangling key contributions to the magnetic interactions at the interface of this oxide heterostructure. For instance, we will show that ferromagnetic  $\text{Ni}^{2+}$ - $\text{O}^{2-}$ - $\text{Mn}^{4+}$  interaction at the interface is observed below 180 K and before the onset of the AFM order in the NNO layer. Also, the exchange bias effect is observed below the paramagnetic to antiferromagnetic transition of NNO at  $T_N = 50$  K, after field cooling the sample in an external magnetic field. Thus, we will be able to conclude that the exchange bias is related to the onset of an AFM ordering of NNO, governed by the exchange coupling between the constituent antiferromagnetic  $\text{Ni}^{3+}$  and Nd ions, and the ferromagnetic LSMO layer that shares a common interface with the NNO layer. The interfacial magnetic frustration will be inferred from the occurrence of mixed ferromagnetic and antiferromagnetic ordering, supporting also possible spin-glass states formed at the LSMO/LNO [12,25],  $\text{LaMnO}_3/\text{LNO}$  [36–38], and LSMO/ $\text{SrMnO}_3$  interfaces [39].

## II. SAMPLES DESCRIPTION AND EXCHANGE BIAS EFFECT IN LSMO/NNO

LSMO/NNO bilayers have been prepared by a pulsed laser deposition system at MESA<sup>+</sup>, University of Twente, The Netherlands using an ultrahigh-vacuum chamber. NNO

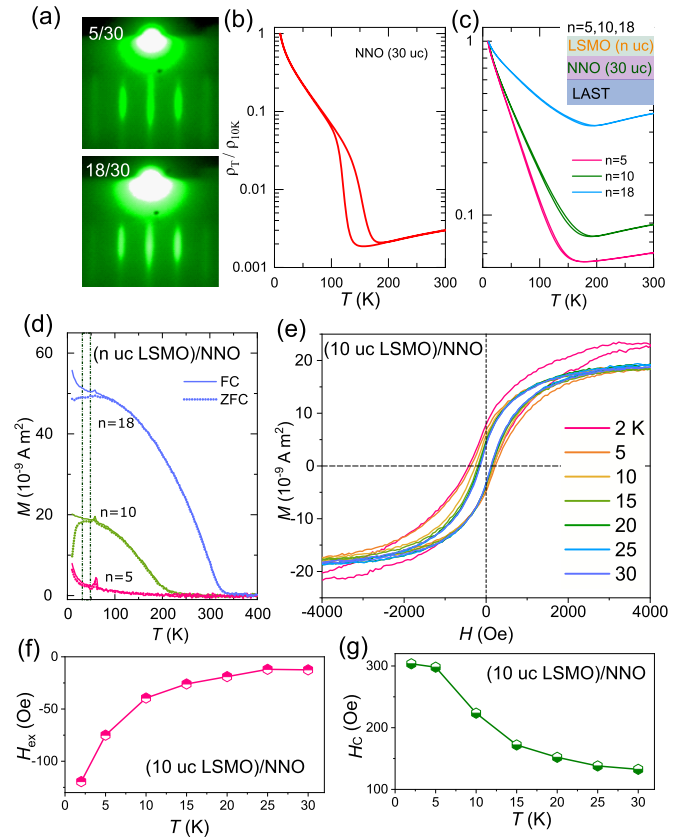


FIG. 1. (a) *In situ* RHEED characterization of the oxide heterostructures for (5 uc LSMO)/NNO and (18 uc LSMO)/NNO grown on LSAT(001) substrates and the  $T$ -dependent resistance measurement as the evidence of Mott transition in bare NNO (b) and LSMO/NNO bilayers (c). (d)  $M$ - $T$  curve for LSMO/NNO bilayers for ZFC/FC conditions. The dashed area highlighting the modification in magnetism below 50 K, and (e) the  $M$ - $H$  hysteresis loops for (10 uc LSMO)/NNO at various temperatures after the FC procedure, with the variation in exchange bias ( $H_{ex}$ ) (up to 120 Oe at 2 K) and coercivity field ( $H_c$ ) as a function of temperature shown in (f) and (g), respectively.

films with constant thickness equal to 30 unit cells (uc) were deposited onto  $(\text{LaAlO}_3)_{0.3}(\text{Sr}_2\text{TaAlO}_6)_{0.7}$  (LSAT) (001) substrates. The ferromagnetic LSMO layer with thicknesses of 5, 10, and 18 uc were deposited on top, therefore sharing a common interface with the antiferromagnetic NNO layer. Both constituent films were grown at 700 °C, in an oxygen pressure of 0.2 mbar and for a laser fluence which was set to  $\sim 2$  J/cm<sup>2</sup>.

Structural characterization of the oxide bilayers has been carried out using reflection high-energy electron diffraction (RHEED) [Fig. 1(a)], x-ray diffraction, and atomic force microscopy (not shown), suggesting that a high structural quality has been achieved for all the oxide heterostructures. Figures 1(b) and 1(c) show the electrical transport measurements of the 30 uc NNO reference layer and of the oxide bilayer samples, which were performed in a van der Pauw geometry using a constant current source. The transport measurements demonstrate the occurrence of the MIT for all bilayer samples, showing that its transition temperature takes place at about

120 K. Notice that the pronounced irreversible nature of the MIT for bare NNO, seen as a broad thermal hysteresis of the resistivity measurements, is strongly diminished for all investigated oxide LSMO/NNO bilayers.

The magnetization as a function of temperature after zero-field cooling (ZFC) and field-cooling (FC) procedures has been recorded using a Quantum Design superconducting quantum interference device magnetometer. The field cooling and measuring field were both set to 500 Oe and the results are shown in Fig. 1(d). The Curie temperatures  $T_c$  are about 70, 180, and 290 K for ( $n$  uc LSMO)/NNO with  $n = 5, 10, \text{ and } 18$ , respectively. Besides the ferromagnetic behavior which originates from the top LSMO layers, a difference between ZFC magnetization and FC magnetization curves can be observed below 50 K, for all oxide bilayer samples. Using a vibrating sample magnetometer (VSM), magnetic hysteresis loops for the (10 uc LSMO)/NNO sample have been measured from 2 to 30 K, after field cooling the sample in an external field of 5000 Oe along the [100] direction, as shown in Fig. 1(e). An exchange bias field ( $H_{ex}$ ) as well as an enhanced coercive field ( $H_C$ ) were observed and they are both increasing as the temperature decreases, as shown in Figs. 1(f) and 1(g), respectively. Note that the exchange bias field ceases to exist at about 30 K, which is lower as compared to the critical temperature where the ZFC and FC curves deviate from each other (50 K). It can be assumed that 50 K corresponds to the Néel temperature of the NNO and that 30 K corresponds to the blocking temperature for the exchange bias effect [24]. This will be confirmed later in the paper by measuring the Néel temperature of the NNO within an element-specific susceptibility approach.

### III. CHARGE TRANSFER AND METAL-INSULATOR TRANSITION

To shed light on the interfacial magnetic contributions to the exchange bias and enhanced coercive field observed for the oxide bilayer, we performed XAS as well as the XMCD measurements at the  $3d$  transition metal (Ni, Mn)  $L_{2,3}$  edges and at the  $M_{4,5}$  edges of Nd, as a function of temperature and for external magnetic fields up to 8 T. XAS was measured in total electron yield (TEY) mode with the photon polarization parallel ( $E \parallel ab$ ) to the samples to determine the valence states of Mn and Ni ions. The dichroic XMCD signal was recorded as the difference of the x-ray absorption spectra measured under a magnetic field of  $\mu_0 H = 8$  T applied perpendicular to the sample surface, with a parallel ( $\sigma^+$ ) and antiparallel ( $\sigma^-$ ) circular helicity beam. Note that the bare XAS spectra which serve as a probe for the MIT were measured with linear polarized beams. The XAS and XMCD spectra were recorded at the VEKMAG end station installed at the PM2 beamline, BESSY II, HZB [40].

The information on the unoccupied Mn and Ni  $3d$  states as well as the related valence states can be deduced from their  $L$ -edge absorption spectra, as shown in Figs. 2(a) and 2(b), respectively. For Mn, the spectra correspond to on-site transitions from  $2p^6 3d^n$  to  $2p^5 3d^{n+1}$  and show two groups of multiplets, namely, the  $L_3$  (641–645 eV) and  $L_2$  (652–656 eV) white line regions, split by the spin-orbit interaction of the Mn  $2p$  core level. We find a significant difference between

the Mn XAS (at 300 K) for (5 uc LSMO)/(NNO) ( $X$  curve) and (10 uc LSMO)/NNO ( $Y$  curve) (normalized by the edge jump) with the former one being shifted towards higher energy values. This is indicative for different valence states carried by the Mn ions in these samples. Since the TEY mode is more sensitive to the surface, more interfacial information contributes to the spectra of the (5 uc LSMO)/NNO sample. The shift of 0.6 eV for sample (5 uc LSMO)/NNO suggests for a higher contribution of  $\text{Mn}^{4+}$  at the interface. This result clearly indicates that a valence gradient of Mn ions in LSMO occurs, with a higher valence at the interface and a lower valence in the outermost monolayers.

The XAS of the Ni  $L$  edge at 10 K for the NNO and for a NiO reference sample are shown in Fig. 2(b). These spectra contain also the La- $M_4$  white lines located at 850.6 eV which have been removed for the consequent analysis. The XAS spectra at the  $L_{2,3}$  edge of the transition-metal oxides are highly sensitive to the valence state with an expected energy shift of more than 1 eV [41] between the spectra of  $\text{Ni}^{2+}$  of NiO and  $\text{Ni}^{3+}$  of  $\text{NdNiO}_3$ . Here, the Ni  $L_3$  main peak exhibits the same position as NiO with an octahedral-coordination oxygen environment, suggesting that the main contribution corresponds to the  $\text{Ni}^{2+}$  ( $3d^7$ ) configuration. The  $\text{Ni}^{3+}$  contribution from the deeper NNO monolayers is also visible as a shoulder at a higher energy equal to 854 eV. Two separated peaks can also be well observed at the Ni  $L_2$  edge, at the same energy of  $\text{Ni}^{2+}$ . These two peaks may originate from the interfacial  $\text{Ni}^{2+}$  or from deeper NNO monolayers with insulating  $\text{Ni}^{3+}$  states. A temperature-dependent XAS investigation across the MIT will help to resolve the origin of the two possible contributions to the double peak at the Ni  $L_2$  edge. Since the leading shoulder peak will disappear for the metallic  $\text{Ni}^{3+}$  states, a variation of their relative weights will provide a self-consistent separation of those components. At this stage, corroborating the higher Mn valence at the interface and the formation of  $\text{Ni}^{2+}$ , we are able to confirm that a charge transfer occurs from Mn cations to Ni cations at the LSMO/NNO interface, fulfilling the charge balance requirement.

Although the main contribution of the Ni  $L_{2,3}$ -edge XAS is from the  $\text{Ni}^{2+}$  formed at the interface of LSMO/NNO, one can still extract the information about the MIT of the buried NNO monolayers from the change of the XAS line shape as a function of temperature. The temperature-dependent spectra of the Ni  $L_3$ -edge XAS (after removing the La  $M_4$  edge) are shown in Fig. 2(c). When compared to the spectra recorded at 300 K, the spectra measured at 10 K show a well separated shoulder peak at the energy of 853 eV. This type of peak splitting is observed throughout the nickelate series and has been associated with the charge-transfer energy separating the O  $2p$  and Ni  $3d$  states near the Fermi level [42]. In Fig. 2(c),  $H_a$  and  $H_b$  are marked by lines, representing the height of the valley and the peak height for the shoulder structure. The temperature dependence of the ratio  $H_b/H_a$  is shown in Fig. 2(e). Upon cooling, it exhibits a rapid increasing below 120 K, in agreement with the MIT temperature obtained from the  $[d \ln R / d \ln(1/T)]$  vs  $T$  curve shown in the inset. This can be due to an increase of the gap between the valence and conduction electrons bands or due to the delocalization of the two bands ( $3d^7$  and  $3d^8 \underline{L}$ ) when entering into the insulator

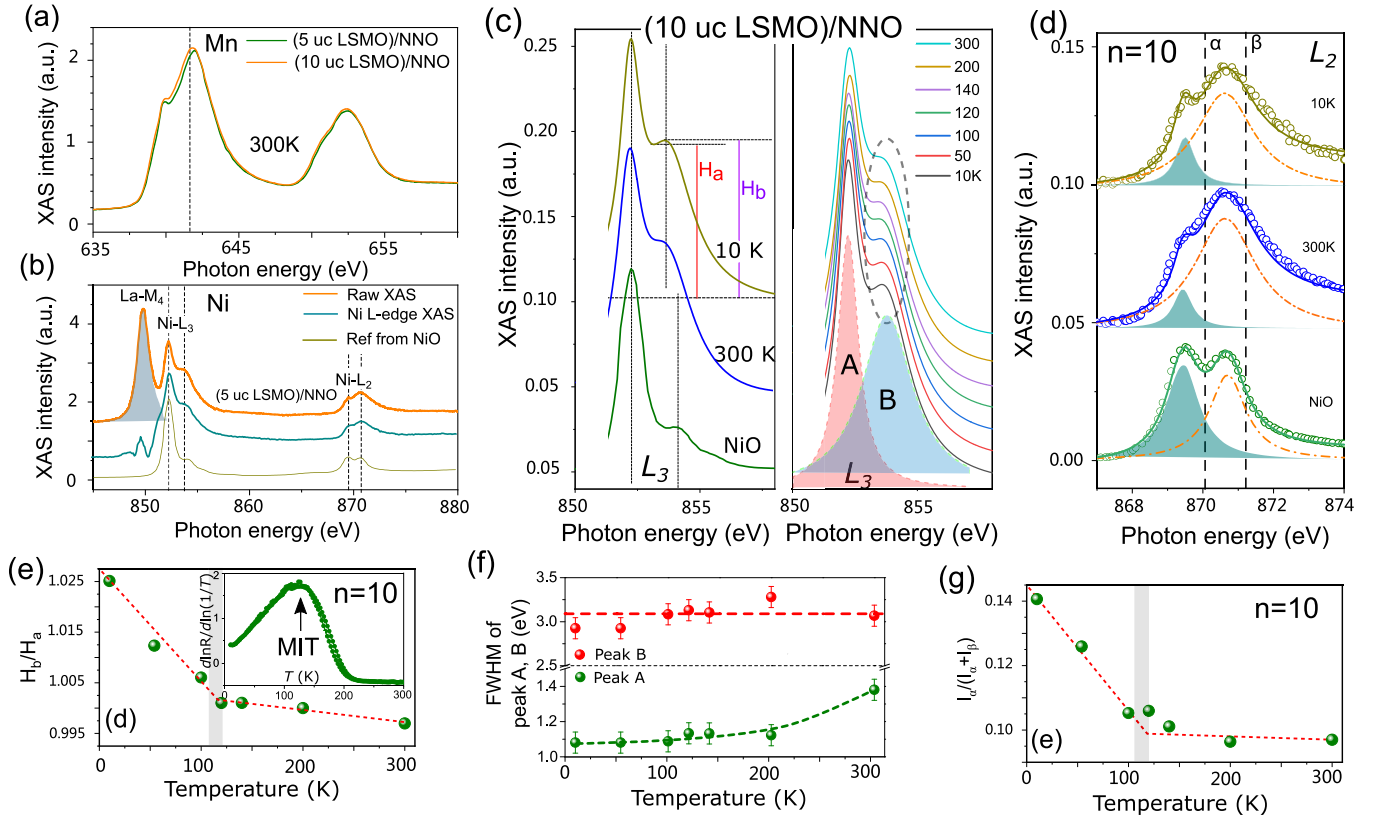


FIG. 2. XAS measured in total electron yield mode of Mn (a) and Ni (b) ions, with an observable difference between the Mn XAS for (5 uc LSMO)/NNO and (10 uc LSMO)/NNO. After removing the La- $M_4$  white lines from Ni XAS, the main contribution with the  $\text{Ni}^{2+} 3d^7$  configuration at the interface is confirmed when comparing to the spectra from NiO. (c) Temperature-dependent  $L_3$ -XAS spectra of Ni cations, with a well separated shoulder peak at the energy of 853 eV at lower temperatures. (e) The temperature dependence of the value of  $H_b/H_a$  follows the MIT from the  $[d \ln R/d \ln(1/T)]$  vs  $T$  curve (inset), with  $H_a$  and  $H_b$  representing the height of the valley and peak for the shoulder structure marked in (c), and (f) the temperature dependence of the width for peaks A and B. (d)  $L_2$ -XAS spectra of the Ni cations at 10 and 300 K and NiO, can be well reproduced from two separated peaks ( $\alpha$ ,  $\beta$ ) with the Lorentzian shape and (g) the temperature dependence of the value for  $I_\alpha/(I_\alpha + I_\beta)$ , with  $I_\alpha$  and  $I_\beta$  representing the peak area of features  $\alpha$  and  $\beta$ , respectively.

phase, which leads to well separated peaks and to an enhanced peak to valley ratio  $H_b/H_a$ . The  $L_3$ -edge XAS can be well fitted with two Lorentzian-shaped components, marked as peak A and peak B in Fig. 2(c). We observe that the full width at half maximum (FWHM) of peak A does significantly change as a function of temperature, whereas the FWHM of peak B remains rather constant within the analysis accuracy. Also, the energy difference between the peak positions is not changing from 300 to 10 K (not shown). These results suggest that through the MIT of the bulk NNO, the reduced mixing of  $d^7$  and  $d^8L$  at the interface is due to the delocalization of the first component only, which is also consistent with the analysis at the  $L_2$  edge which is described further below.

Similar to the  $L_2$ -edge XAS of NiO, two well separated Lorentzian-shaped peaks ( $\alpha$ ,  $\beta$ ) can well reproduce the XAS spectra of the Ni cations at the interface, as shown in Fig. 2(d). Note that both  $\text{Ni}^{2+}$  and  $\text{Ni}^{3+}$  may contribute to these two peaks of  $\alpha$  and  $\beta$  [43]. Since no valence change has been observed for Mn sites between 10 and 300 K, we assume that the valence of Ni sites at the interface remains unchanged through the MIT. Considering that the contribution to the  $\alpha$  peak by  $\text{Ni}^{2+}$  remains constant as a function of the temperature, then the temperature variation of the  $\alpha$  peak intensity is due to the

MIT of the  $\text{Ni}^{3+}$  in the buried NNO monolayers. This scenario is also supported by the temperature dependence of the peak increase of the  $\alpha$  peak intensity at lower temperature can be observed according to the value of  $I_\alpha/(I_\alpha + I_\beta)$ , where  $I_\alpha$  and  $I_\beta$  represent the peak area of  $\alpha$  and  $\beta$  peaks, respectively. The change of  $I_\alpha/(I_\alpha + I_\beta)$  as a function of temperature is shown in Fig. 2(g). Its variation as a function of temperature agrees with the character of  $H_b/H_a$  shown in Fig. 2(e), revealing that the same MIT occurs for the deeper NNO monolayers.

#### IV. EXCHANGE COUPLING AT THE INTERFACE

Having established the valence of the  $\text{Mn}^{4+}$  and  $\text{Ni}^{2+}$  at the interface of LSMO/NNO, as expected from the charge-transfer scenario, we evaluate in this section the interfacial exchange coupling behavior by exploring the element-specific XMCD spectra of Mn, Ni, as well as of the Nd ions. The normalized XAS of Mn  $L_{2,3}$ , Ni  $L_{2,3}$ , and Nd  $M_{4,5}$  and the related XMCD spectra for the sample of (10 uc LSMO)/NNO recorded at 10 K and  $\mu_0 H = 8$  T are shown in Figs. 3(a)–3(c), respectively. The negative XMCD sign at both the Mn and the Ni  $L_3$  edges, indicates that the  $\text{Ni}^{2+}$  and  $\text{Mn}^{4+}$  ions are aligned

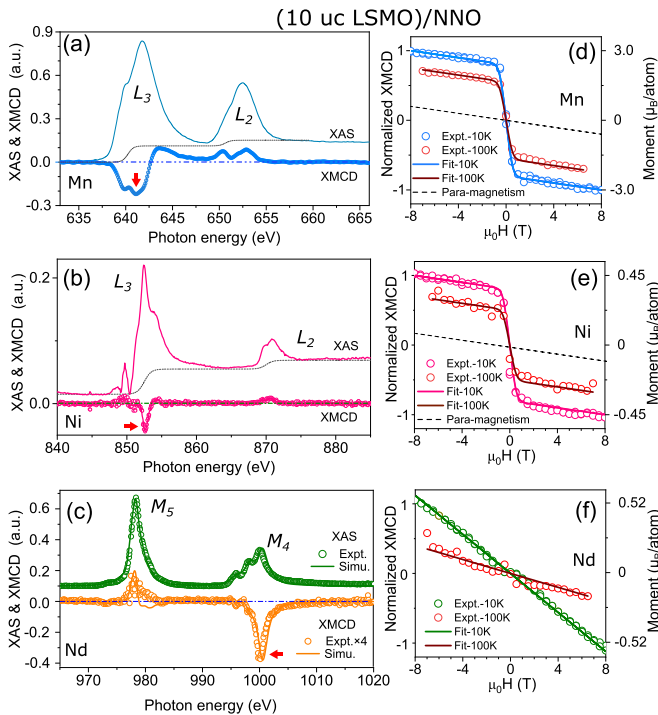


FIG. 3. (a)–(c) XAS spectra of Mn  $L_{2,3}$ , Ni  $L_{2,3}$ , and Nd  $M_{4,5}$  edges and the related XMCD spectra for the sample of 10 uc LSMO/NNO recorded at 10 K and  $\mu_0 H = 8$  T; (d)–(f) the element-specific magnetic hysteresis loop, recorded as the field-dependent XMCD intensity at Mn, Ni, and Nd edges [see red marks in (a)–(c)] for  $T = 10$  and 100 K. Multiplet simulations of XAS and XMCD for  $\text{Nd}^{3+}$  are also shown in (c) together with the experimental spectra.

ferromagnetically in agreement with a positive sign of the  $\text{Mn}^{4+}\text{-O}^{2-}\text{-Ni}^{2+}$  superexchange interaction at the interface, similar to that observed in  $\text{La}_2\text{NiMnO}_6$  [21,22]. Noncollinear magnetic order of  $\text{Nd}^{3+}$  in epitaxial  $\text{NdNiO}_3$  film has been inferred from resonant soft x-ray diffraction [44]. Here, the  $M_{4,5}$  edge XAS and XMCD spectra have been measured to investigate the magnetic properties of the Nd ions. The  $M_{4,5}$  edge XAS spectra [Fig. 3(c)] at the interface show the same multiplet structures as obtained through numerical simulations for the  $\text{Nd}^{3+}$  [45]. The positive and negative signals of the XMCD spectra at the  $M_5$  and  $M_4$  edges is due to the antiparallel alignment between the orbital and spin moments of Nd. The orbital magnetic moments, which are higher in absolute value as compared to the spin moments, are pulled parallel to the external field.

XMCD sum rules [46,47] have been applied to both the Ni and Mn spectra. The orbital moments are close to zero for both elements, since they are known to be quenched by the crystal field. For the analysis of the Ni moments we use a number of holes equal to  $n_h = 2.2$ , which lies in between the value of 2.5 for  $\text{Ni}^{3+}$  in nickelates [48] and 1.8 for  $\text{Ni}^{2+}$  [49]. The total magnetic moment of Ni  $M = M_S + M_L$  is determined to be  $0.45 \pm 0.10 \mu_B/\text{Ni}$  at 10 K and  $\mu_0 H = 8$  T, which is much higher as compared to the reported value for the LMO/LNO interface. Notice that the same correction factor of 1.1 was used to correct for the mixing of the  $L_3$  and  $L_2$  edges of Ni [50]. For Mn, we used  $n_h = 6.0$ , which

lies in between the value of 5.5 for  $\text{Mn}^{3+}$  and 6.4 for  $\text{Mn}^{4+}$  [49]. The total moment of Mn  $M = M_S + M_L$  is determined to be  $3.0 \pm 0.20 \mu_B/\text{Mn}$  at 10 K and  $\mu_0 H = 8$  T, similar to the value of Mn moments in the LMO/LNO interface when the same correction factor of 1.7 is used as in Ref. [50].

For Nd  $M_{4,5}$  edges the sum rules [46,47] cannot confidently be applied without considering additional correction factors [51]. Therefore, atomic multiplet calculations [Fig. 3(c)] using the QUANTY code [52,53] have been performed to obtain the spin and orbital moments for Nd. The experimental XAS spectrum was well reproduced by the simulations when considering a  $4f^3$  ( $L = 6$ ,  $S = 3/2$ ,  $J = L - S = 9/2$ ) ground-state configuration. After scaling the measured XMCD spectrum (at 10 K) by a factor of 4, the simulated XMCD spectra overlaps very well with the experimental data. The full saturated expectation values for  $\text{Nd}^{3+}$  ions are  $M_L = 3.8$ ,  $M_S = -2.2$ , and  $M = 1.6 \mu_B/\text{atom}$ . By matching the experimental and the simulated spectra we obtain a total magnetic moment  $M = 0.52 \mu_B/\text{Nd}$  with the orbital (spin) moment equal to 1.23 ( $-0.71$ )  $\mu_B$  aligned parallel (antiparallel) to the field. These values suggest that Nd net moment cannot be fully saturated within the available magnetic fields due to its intrinsic antiferromagnetic ordering.

The element-specific magnetic hysteresis loops, recorded as the field-dependent XMCD intensity at Mn  $L_3$ , Ni  $L_3$ , and Nd  $M_4$  edges [see red marks in Figs. 3(a)–3(c)], are shown in Figs. 3(d)–3(f) for  $T = 10$  and 100 K. The similarity of the hysteresis loop shape measured for Mn and Ni demonstrates a strong ferromagnetic coupling between the Mn and the Ni cations at the interface, for both  $T = 10$  and 100 K temperatures. Because NNO is antiferromagnet at low temperatures, the ferromagnetic ordering of Ni cations as well as their high magnetic moment can only be located at the interface in these heterostructures.

In contrast, only linear magnetic response was observed for Nd cations for  $T = 10$  and 100 K. The linear dependence of the element-specific magnetization as a function of the magnetic field suggests either a paramagnetic or an antiferromagnetic behavior for the Nd moments. This is different when compared to the ferromagnetic behavior of Ni and Mn cations at the interface. To distinguish between these two scenarios, temperature dependence of the interfacial magnetic susceptibility needs to be performed, which will be described further below.

The XMCD intensities measured at  $\mu_0 H = 8$  T for the Nd  $M_4$ , Mn  $L_3$ , and Ni  $L_3$  edges as a function of temperature ranging from 10 to 100 K are shown in Figs. 4(a)–4(c). For Mn and Ni cations, the curves follow the VSM curve of the (10 uc LSMO)/NNO sample [see Fig. 1(c)], and can be well fitted with  $M \propto (T_c - T)^\beta$  with the exponent  $\beta = 0.31$  and  $T_c = 180$  K. To establish the antiferromagnetic ordering of the NNO layer, we have measured the magnetization of the Nd element as a function of temperature, as shown in Fig. 4(a). We observe that the magnetization deviates significantly from an inverse linear behavior at 50 K. Plotting the inverse of the XMCD intensity as a function of temperature, shown in the inset of Fig. 4, we observe a typical behavior of a magnetic susceptibility character, where deviations from a paramagnetic linear behavior are indicative for a paramagnetic to antiferromagnetic phase transition. As such, we are able to

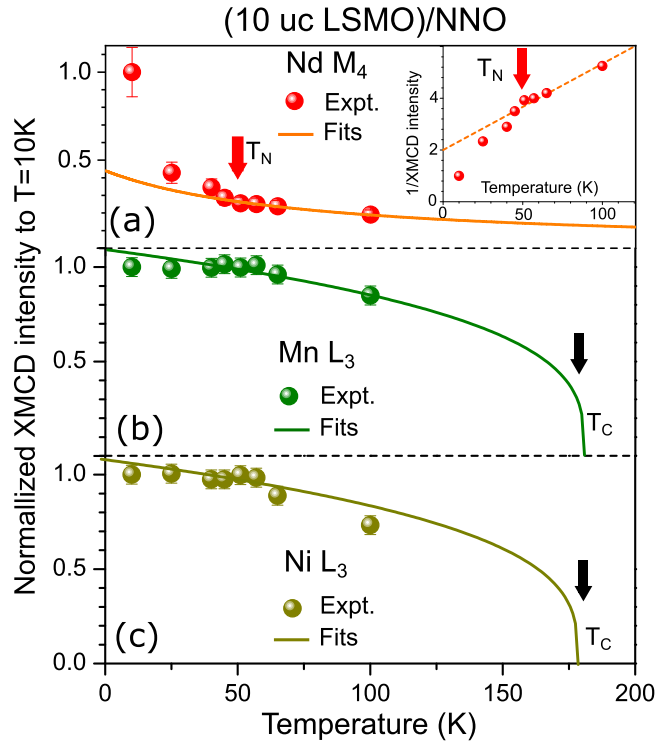


FIG. 4. (a)–(c) The XMCD intensity measured at  $\mu_0 H = 8$  T for Nd  $M_4$ , Mn  $L_3$ , and Ni  $L_3$  edges, varying the temperature from 10 to 100 K. For Mn and Ni cations, the curves can be well fitted with  $M \propto (T_c - T)^\beta$  with the exponent  $\beta = 0.31$  and  $T_c = 180$  K. For Nd ions, the canting moment is continuously increasing from 100 to 50 K following the curve of  $M \propto 1/(T - \theta)$  with  $\theta = -75$  K, while the inverse of the XMCD intensity [inset of Fig. 4(a)] deviates from the linear response at  $T = 50$  K, which is the antiferromagnetic ordering temperature of the NNO films.

conclude that the onset of an antiferromagnetic ordering of the buried NNO films takes place and the Néel temperature of NNO, which is determined to be 50 K.

Note that the temperature dependence of the magnetization of the NNO layer, recognized also as different slopes for the 10 and 100 K magnetization curves shown in Fig. 3(f), help to resolute on the nature of the linear increase of magnetization for the Ni and Mn hysteresis loops at high fields [see Figs. 3(d) and 3(e)]. The slope of the hysteresis loop for Ni and Mn at high fields is not changing as a function of temperature. This suggests that coupling to the NNO layer is not likely to be the origin of this slope, otherwise it would change across the Néel temperature, similar to the slope change which is characteristic to the AF layer. This further indicates that the most plausible origin of this slope can reside in antiferromagnetic correlations of Mn, belonging to the LSMO layer itself. They can be located at the interface due to a variation of the Mn valence, or even be part of the LSMO layer as a concurrent phase to the ferromagnetic ordering. Note that discussions on a similar effect which was observed for the LSMO/LNO system, left its origin open [16,50].

The  $T_{MIT}$  and  $T_N$  were reported to be equal ( $\sim 180$  K) for bulk NNO [54] crystals. For thin films, both the  $T_{MIT}$  and  $T_N$  are reduced, with  $T_N \leq T_{MIT}$  [55]. In our case,  $T_N = 50$  K is far below the  $T_{MIT} = 120$  K. Therefore, the exchange bias effect which was only observed below a blocking temperature of 30 K, is related to the paramagnetic-antiferromagnetic transition of the NNO layer. The  $Ni^{2+}$  at the interface can rotate due to the exchange interaction with the Mn element which can further be reversed by a relatively low external magnetic fields. Besides, the maximum of the exchange bias field for LSMO/NNO is around 120 Oe which suggests that the pinned spins responsible for the exchange bias are reduced at the interface. As reported recently, using different substrates, it is possible to tune the charge transfer and magnetism at the NNO/LSMO interface [20]. According to the charge-transfer scenario, an electron is donated from Mn to Ni to form  $Mn^{4+}-O-Ni^{2+}$ . On the one hand, one may observe a reduced magnetization, since the saturated magnetization of  $Mn^{4+}$  ( $S = 3/2$ ) is weaker as compared to  $Mn^{3+}$  ( $S = 2$ ). On the other hand, the ferromagnetic  $Ni^{2+}$  with the moment of  $0.45\mu_B/\text{atom}$  is formed at the interface replacing some of the antiferromagnetic  $Ni^{3+}$ , and therefore providing an even further reduction for the unidirectional anisotropy and favoring the occurrence of loose interfacial spins responsible for an enhanced coercive field as shown in Fig. 1(g).

## V. CONCLUSIONS

In conclusion, using soft x-ray spectroscopy and XMCD in high magnetic fields we have shown that interfacial charge transfer from  $Mn^{3+}$  in LSMO to  $Ni^{2+}$  in NNO drives a ferromagnetic coupling  $Ni^{2+}-O^{2-}-Mn^{4+}$  at the LSMO/NNO interface. Analyzing the line-shape changes of the temperature-dependent XAS spectra, the MIT was resolved and its temperature onset was determined to be  $T_{MIT} = 120$  K. The occurrence of antiferromagnetic phase of the NNO layer was established and characterized by element-specific magnetic susceptibility measurements. The onset of the AF order was measured to occur at the Néel temperature equal to  $T_N = 50$  K. A ferromagnetic coupling between the interfacial  $Ni^{2+}$  and the  $Ni^{3+}$  ions is observed, with the latter being antiferromagnetically ordered in the deeper NNO monolayers. Our findings strongly suggest that the interfacial charge transfer plays an important role for the interfacial magnetism and can be used for tuning the magnetic properties of the upper ferromagnetic layers. The exchange bias effect observed in this system, below  $T = 30$  K, is reduced due to the frustrated nature of the interface.

## ACKNOWLEDGMENTS

We thank the HZB for the allocation of synchrotron radiation beamtime. The authors acknowledge the financial support for the VEKMAG project and for the PM2-VEKMAG beamline by the German Federal Ministry for Education and Research (BMBF 05K10PC2, 05K10WR1, and 05K10KE1) and by HZB. Steffen Rudorff is acknowledged for technical support.

- [1] J. Mannhart and D. G. Schlom, *Science* **327**, 1607 (2010).
- [2] A. Brinkman, M. Huijben, M. van Zalk, J. Huijben, U. Zeitler, J. C. Maan, W. G. van der Wiel, G. Rijnders, D. H. A. Blank, and H. Hilgenkamp, *Nat. Mater.* **6**, 493 (2007).
- [3] M. Basletic, J.-L. Maurice, C. Carretero, G. Herranz, O. Copie, M. Bibes, E. Jacquet, K. Bouzehouane, S. Fusil, and A. Barthelemy, *Nat. Mater.* **7**, 621 (2008).
- [4] Julie A. Bert, Beena Kalisky, Christopher Bell, Minu Kim, Yasuyuki Hikita, Harold Y. Hwang, and Kathryn A. Moler, *Nat. Phys.* **7**, 767 (2011).
- [5] Lu Li, C. Richter, J. Mannhart, and R. C. Ashoori, *Nat. Phys.* **7**, 762 (2011).
- [6] A. Ohtomo and H. Y. Hwang, *Nature (London)* **427**, 423 (2004).
- [7] Y. Z. Chen, N. Bovet, F. Trier, D. V. Christensen, F. M. Qu, N. H. Andersen, T. Kasama, W. Zhang, R. Giraud, J. Dufouleur, T. S. Jespersen, J. R. Sun, A. Smith, J. Nygard, L. Lu, B. Büchner, B. G. Shen, S. Linderoth, and N. Pryds, *Nat. Commun.* **4**, 1371 (2013).
- [8] H. J. Lee, T. Moon, C. H. An, and C. S. Hwang, *Adv. Electron. Mater.* **5**, 1800527 (2019).
- [9] M. Sirena, N. Haberkorn, M. Granada, L. B. Steren, and J. Guimpel, *J. Appl. Phys.* **105**, 033902 (2009).
- [10] L. Yao, S. Inkinen, and S. van Dijken, *Nat. Commun.* **8**, 14544 (2017).
- [11] H. Guo, J. Wang, X. He, Z. Yang, Q. Zhang, K.-j Jin, C. Ge, R. Zhao, L. Gu, Y. Feng, W. Zhou, X. Li, Q. Wan, M. He, C. Hong, Z. Guo, C. Wang, H. Lu, K. Ibrahim, S. Meng, H. Yang, and G. Yang, *Adv. Mater. Interfaces* **3**, 1500753 (2016).
- [12] J. Peng, C. Song, F. Li, B. Cui, H. Mao, Y. Wang, G. Wang, and F. Pan, *ACS Appl. Mater. Interfaces* **7**, 17700 (2015).
- [13] R. Pentcheva and W. E. Pickett, *Phys. Rev. B* **78**, 205106 (2008).
- [14] M. Imada, A. Fujimori, and Y. Tokura, *Rev. Mod. Phys.* **70**, 1039 (1998).
- [15] M. S. Saleem, C. Songa, J. J. Peng, B. Cui, F. Li, Y. D. Gu, and F. Pan, *Appl. Phys. Lett.* **110**, 072406 (2017).
- [16] J. C. Rojas Sanchez, B. Nelson-Cheeseman, M. Granada, E. Arenholz, and L. B. Steren, *Phys. Rev. B* **85**, 094427 (2012).
- [17] G. Zhou, C. Song, Y. Bai, Z. Quan, F. Jiang, W. Liu, Y. Xu, S. S. Dhesi, and X. Xu, *ACS Appl. Mater. Interfaces* **9**, 3156 (2017).
- [18] J. D. Hoffman, B. J. Kirby, J. Kwon, G. Fabbris, D. Meyers, J. W. Freeland, I. Martin, O. G. Heinonen, P. Steadman, H. Zhou, C. M. Schlepütz, M. P. M. Dean, S. G. E. te Velthuis, J.-M. Zuo, and A. Bhattacharya, *Phys. Rev. X* **6**, 041038 (2016).
- [19] G. Zhou, F. Jiang, J. Zang, Z. Quan, and X. Xu, *ACS Appl. Mater. Interfaces* **10**, 1463 (2018).
- [20] Z. Xu, S. Hu, R. Wu, J.-O. Wang, T. Wu, and L. Chen, *ACS Appl. Mater. Interfaces* **10**, 30803 (2018).
- [21] R. I. Dass, J.-Q. Yan, and J. B. Goodenough, *Phys. Rev. B* **68**, 064415 (2003).
- [22] H. Das, U. V. Waghmare, T. Saha-Dasgupta, and D. D. Sarma, *Phys. Rev. Lett.* **100**, 186402 (2008).
- [23] J. Hoffman, I. C. Tung, B. B. Nelson-Cheeseman, M. Liu, J. W. Freeland, and A. Bhattacharya, *Phys. Rev. B* **88**, 144411 (2013).
- [24] F. Radu and H. Zabel, *Springer Tracts Mod. Phys.* **227**, 97 (2008).
- [25] X. Ning, Z. Wang, and Z. Zhang, *Sci. Rep.* **5**, 8460 (2015).
- [26] D. Kumar, K. P. Rajeev, A. K. Kushwaha, and R. C. Budhani, *J. Appl. Phys.* **108**, 063503 (2010).
- [27] J. Liu, M. Kareev, B. Gray, J. W. Kim, P. Ryan, B. Dabrowski, J. W. Freeland, and J. Chakhalian, *Appl. Phys. Lett.* **96**, 233110 (2010).
- [28] Jian Liu, M. Kargarian, M. Kareev, B. Gray, P. J. Ryan, A. Cruz, N. Tahir, Y.-D. Chuang, J. Guo, J. M. Rondinelli, J. W. Freeland, G. A. Fiete, and J. Chakhalian, *Nat. Commun.* **4**, 2714 (2013).
- [29] R. S. Dhaka, T. Das, N. C. Plumb, Z. Ristic, W. Kong, C. E. Matt, N. Xu, K. Dolui, E. Razzoli, M. Medarde, L. Patthey, M. Shi, M. Radovic, and J. Mesot, *Phys. Rev. B* **92**, 035127 (2015).
- [30] L. Wang, S. Ju, L. You, Y. Qi, Y.-w. Guo, P. Ren, Y. Zhou, and J. Wang, *Sci. Rep.* **5**, 18707 (2015).
- [31] S. Heo, C. Oh, M. J. Eom, J. S. Kim, J. Ryu, J. Son, and H. M. Jang, *Sci. Rep.* **6**, 22228 (2016).
- [32] M. K. Hooda and C. S. Yadav, *Physica B* **491**, 31 (2016).
- [33] N. Palina, L. Wang, S. Dash, X. Yu, Mark B. H. Breese, J. Wang, and A. Rusydi, *Nanoscale* **9**, 6094 (2017).
- [34] T. Onozuka, A. Chikamatsu, T. Katayama, Y. Hirose, I. Harayama, D. Sekiba, E. Ikenaga, M. Minohara, H. Kumigashira, and T. Hasegawa, *ACS Appl. Mater. Interfaces* **9**, 10882 (2019).
- [35] J. Li, J. Pellicciari, C. Mazzoli, S. Catalano, F. Simmons, J. T. Sadowski, A. Levitan, M. Gibert, E. Carlson, J.-M. Triscone, S. Wilkins, and R. Comin, *Nat. Commun.* **10**, 4568 (2019).
- [36] A. T. Lee and M. J. Han, *Phys. Rev. B* **88**, 035126 (2013).
- [37] M. Gibert, M. Viret, P. Zubko, N. Jaouen, J.-M. Tonnerre, A. Torres-Pardo, S. Catalano, A. Gloter, O. Stephan, and J.-M. Triscone, *Nat. Commun.* **7**, 11227 (2016).
- [38] J. Zang, G. Zhou, Y. Bai, Z. Quan, and X. Xu, *Sci. Rep.* **7**, 10557 (2017).
- [39] J. F. Ding, O. I. Lebedev, S. Turner, Y. F. Tian, W. J. Hu, J. W. Seo, C. Panagopoulos, W. Prellier, G. Van Tendeloo, and T. Wu, *Phys. Rev. B* **87**, 054428 (2013).
- [40] T. Noll and F. Radu, *Proceedings of Mechanical Engineering Design of Synchrotron Radiation Equipment and Instrumentation Conference (MEDSI'16), 11-16 September 2016, Barcelona, Spain* (JACoW, Geneva, Switzerland, 2017), pp. 370–373.
- [41] H. Guo, Z. W. Li, L. Zhao, Z. Hu, C. F. Chang, C.-Y. Kuo, W. Schmidt, A. Piovano, T. W. Pi, O. Sobolev, D. I. Khomskii, L. H. Tjeng, and A. C. Komarek, *Nat. Commun.* **9**, 43 (2018).
- [42] J. W. Freeland, M. van Veenendaal, and J. Chakhalian, *J. Electron. Spectrosc. Relat. Phenom.* **208**, 56 (2016).
- [43] J. Liu, S. Okamoto, M. van Veenendaal, M. Kareev, B. Gray, P. Ryan, J. W. Freeland, and J. Chakhalian, *Phys. Rev. B* **83**, 161102(R) (2011).
- [44] V. Scagnoli, U. Staub, Y. Bodenthin, M. García-Fernández, A. M. Mulders, G. I. Meijer, and G. Hammerl, *Phys. Rev. B* **77**, 115138 (2008).
- [45] B. T. Thole, G. van der Laan, and G. A. Sawatzky, *Phys. Rev. Lett.* **55**, 2086 (1985).
- [46] B. T. Thole, P. Carra, F. Sette, and G. van der Laan, *Phys. Rev. Lett.* **68**, 1943 (1992).
- [47] P. Carra, B. T. Thole, M. Altarelli, and X. Wang, *Phys. Rev. Lett.* **70**, 694 (1993).
- [48] V. Scagnoli, U. Staub, A. M. Mulders, M. Janousch, G. I. Meijer, G. Hammerl, J. M. Tonnerre, and N. Stojic, *Phys. Rev. B* **73**, 100409(R) (2006).
- [49] T. Saitoh, A. E. Bocquet, T. Mizokawa, and A. Fujimori, *Phys. Rev. B* **52**, 7934 (1995).

- [50] C. Piamonteze, M. Gibert, J. Heidler, J. Dreiser, S. Rusponi, H. Brune, J.-M. Triscone, F. Nolting, and U. Staub, *Phys. Rev. B* **92**, 014426 (2015).
- [51] Y. Teramura, A. Tanaka, B. T. Thole, and T. Jo, *J. Phys. Soc. Jpn.* **65**, 3056 (1996).
- [52] M. W. Haverkort, G. Sangiovanni, P. Hansmann, A. Toschi, Y. Lu, and S. Macke, *Europhys. Lett.* **108**, 57004 (2014).
- [53] Parameters: Oh symmetry,  $\mu_0 H = 6$  T,  $T = 0.1$  K, the scale factor for Slater integrals of Hartree-Fock values and the spin-orbital couplings are 0.8 and 1, respectively.
- [54] J. B. Torrance, P. Lacorre, A. I. Nazzal, E. J. Ansaldo, and Ch. Niedermayer, *Phys. Rev. B* **45**, 8209(R) (1991).
- [55] A. M. Alsaqqa, S. Singh, S. Middey, M. Kareev, J. Chakhalian, and G. Sambandamurthy, *Phys. Rev. B* **95**, 125132 (2017).